Prediction of Antenna Reflection Coefficient in Presence of Multilayer Media: A Fast Spectral Domain Approach

Ramin Roohi, Amir Reza Attari, Mohammad Saeed Majedi, and Sébastien Lambot, *Member, IEEE*

***Abstract*— Asphalt thickness estimation using ground-penetrating radar (GPR) is an important application in transportation infrastructure inspections. Thin asphalt measurement needs to use super-resolution or full-wave methods to process the GPR signals with overlapped echoes. We propose a model for antenna reflection coefficient in the presence of multilayer medium by omitting considerations of evanescent waves and interactions between the antenna and the medium. We formulated it within the spectral domain, enabling the explicit incorporation of the antenna's radiation pattern. This model is about 100 times faster than the existing full-wave models. In this model, we calculate the plane wave expansion (PWE) of the antenna radiated field. Ignoring the evanescent waves, the PWE of the radiated field is calculated from the far-field pattern of the antenna. Simulation and measurement results confirm the validity and effectiveness of this model in asphalt thickness measurement.**

***Index Terms*— Antenna modeling, ground-penetrating radar (GPR), *k*-space, multilayer, pavement thickness measurement.**

I. Introduction

GROUND-PENETRATING radar (GPR) has important applications in nondestructive testing and evaluation of transportation infrastructures. These applications include pavement layers thickness estimation [1], [2], [3], [4], moisture estimation [5], [6], [7], void detection [8], and density estimation [9], [10], [11]. The most important application of GPR among these applications is the thickness estimation [2], [12], [13]. Furthermore, thickness estimation of layered media is useful in other applications such as underground coal mining [14] or environmental monitoring [15].

The traditional methods for pavement thickness estimation are based on the calculation of two-way travel time (TWTT) of the GPR signal [16], [17]. In this approach, the time difference between the received echoes from the top and bottom surfaces of each layer is utilized for thickness estimation. One of these traditional methods for estimating thickness is using surface reflection coefficients, which utilizes both the TWTT and the amplitude of the received echo signal [3], [18]. Other methods are based on multioffset configurations, such as common source [2] and common midpoint [19], [20]. Lahouar et al. [19] and Leng and Al-Qadi [21] demonstrated that evaluating the thickness and permittivity simultaneously requires only two TWTT data points—one from monostatic and the other from bistatic measurements.

The above-mentioned thickness estimation methods that use the TWTT are not suitable for thin pavement layers where the echoes from the layer interfaces interfere with each other [1]. This situation occurs when the pulsewidth of the incident signal is wide or the time difference between the echoes from the layer interfaces, $\Delta\tau$, is very low [22]. The pulsewidth of the incident signal is inversely proportional to the frequency bandwidth B of the GPR. The methods addressing this problem are called super-resolution methods. As defined quantitatively in [22], super-resolution methods are the methods that can estimate the thickness of layers with a $B\Delta\tau$ product less than 1. These methods include layer stripping [23], deconvolution [24], [25], and high-resolution algorithms, e.g., MUSIC [22] and methods based on machine learning algorithms [26]. Most super-resolution methods rely on a simplified data model to predict the backscattered signal. In this model, the backscattered signal consists of the summation of the echoes. The received signal from each interface is approximated by amplitude scaling and time shifting of the input signal [22], [23]. This model is applicable, when the distance of the antenna from the pavement surface satisfies the far-field conditions [22]. In addition, in this model, the multiple reflections from the multilayer interfaces are neglected. Using full-wave inversion with an exact solution of Maxwell's equations for wave propagation in 3-D multilayered media permits super-resolution reconstruction [27], [28]. Lambot et al. [29] proposed a far-field model (FFM) for the prediction of the backscattered signal that considers the electromagnetic (EM) phenomena in a multilayer medium as well as the antenna and antenna–medium interactions. This model was preceded by Lambot et al. [30], where the antenna–medium interactions were not modeled. Using this model, the full-wave inversion is possible and the complete information of the GPR signal is used. Lambot and André [31] also proposed a near-field model (NFM) to improve the FFM for near-field measurements and implemented it for asphalt thickness measurement

Manuscript received 13 March 2024; revised 6 June 2024; accepted 26 June 2024. Date of publication 10 July 2024; date of current version 8 August 2024. *(Corresponding author: Amir Reza Attari.)*

Ramin Roohi is with the Computer and Communications Research Center, Faculty of Engineering, Ferdowsi University of Mashhad, Mashhad 9177948944, Iran (e-mail: ra.roohi@mail.um.ac.ir).

Amir Reza Attari and Mohammad Saeed Majedi are with the Department of Electrical Engineering, Faculty of Engineering, Ferdowsi University of Mashhad, Mashhad 9177948944, Iran (e-mail: attari50@um.ac.ir; majedi@um.ac.ir).

Sébastien Lambot is with the Earth and Life Institute, Université Catholique de Louvain, 1348 Louvain-la-Neuve, Belgium (e-mail: sebastien.lambot@uclouvain.be).

Digital Object Identifier 10.1109/TGRS.2024.3426316

in [12]. This model also has been used for other applications such as multilayer concrete evaluation [27] and soil moisture content measurement [7], [32]. In these models, the antenna is considered as a point source [29] or multiple point sources [31], and the effect of the antenna is modeled by global reflection and transmission functions that are determined by calibration. These transfer functions model the free space reflection coefficient, the transmitting, receiving, and multiple reflections of the real antenna and convert the point-source analytical response, so-called Green's function, to real radar measurements, e.g., S_{11} in case of a vector network analyzer based radar. The spatial-domain Green's function of multilayer medium for a point source is derived by using the spectral-domain Green's function. Calculation of the spatial-domain Green's function from spectral-domain Green's function involves a complex integral that is time-consuming, especially for bistatic configurations involving Bessel's functions. The calculation time is important because Green's function is used in an optimization procedure and need to be evaluated many times. Lambot et al. [33] proposed an optimal integration path to decrease the calculation time, but it improves the speed only by a factor of about 4. Furthermore, the calculation speed depends on the structure of the multilayer medium [34]. Nevertheless, for simple model configurations involving one layer only, this exact model formulation can already provide real-time inversion capabilities [35] using gprSense (https://www.gprsense.com/). For the reconstruction of multiple layers, however, calculation time is still a limitation.

In this article, we propose an approach to predict the antenna reflection coefficient in the presence of a multilayer medium. In this approach, instead of spatial-domain Green's function of a single or multiple point sources radiated field, we use plane wave (PW) expansion (PWE) of the antenna radiated field. The antenna radiated field derived from this PWE can provide a good prediction of field variations near the antenna. The proposed model is based on the PW scattering matrix (PWSM) theory [36]. In this approach, it is not required to compute a complex integral, and this improves the speed of forward problem solution. We use two assumptions in this approach. First, we neglect the evanescent PWs and second, we neglect the multiple reflections from the antenna-to-multilayer medium. One of the features of the proposed approach is the explicit use of the radiation pattern in the model. In the rest of this article, we first explain the theory of the proposed approach and present its implementation for an arbitrary multilayer medium in Section II. Also, in this section, we explain the existing full-wave model in order to compare it with our approach. Next, we verify the validity of this approach by the simulation and compare it with the FFM in Section III. Finally, in Section IV, we apply the approach for estimation of the asphalt thickness using simulation and measurement data.

II. Theory

A. Multilayer Medium Response to Plane Wave

In accordance with the theory of reflection and transmission of layered medium [37], [38], we consider a multilayer medium that consists of N layers, as depicted in Fig. 1. For upward and downward propagating PWs, the wave vectors are $\boldsymbol{k} = k_x\hat{\boldsymbol{x}} + k_y\hat{\boldsymbol{y}} + k_z\hat{\boldsymbol{z}}$ and $\boldsymbol{k} = k_x\hat{\boldsymbol{x}} + k_y\hat{\boldsymbol{y}} - k_z\hat{\boldsymbol{z}}$, respectively, where $k_z = (k^2 - k_x^2 - k_y^2)^{1/2}$. The plane containing the k-vector of the incident PW and $\hat{z}$ is called the incidence plane. The electric field of a PW is perpendicular to its wave vector $\boldsymbol{k}$ and can be projected into transverse electric (TE) and transverse magnetic (TM) polarizations. In TE polarization, electric field is perpendicular to the incidence plane and in TM polarization, electric field is parallel to the incidence plane. The reflection coefficients of TE and TM polarizations from the multilayer medium are determined using recursive relations [38]

$$r_n^{\mathrm{TE}} = \frac{E_\perp^{\mathrm{reflected}}}{E_\perp^{\mathrm{incident}}} = \frac{\mu_{n+1}k_{z,n} - \mu_n k_{z,n+1}}{\mu_{n+1}k_{z,n} + \mu_n k_{z,n+1}} \tag{1}$$

$$r_n^{\mathrm{TM}} = \frac{H_\perp^{\mathrm{reflected}}}{H_\perp^{\mathrm{incident}}} = \frac{\varepsilon_{n+1}k_{z,n} - \varepsilon_n k_{z,n+1}}{\varepsilon_{n+1}k_{z,n} + \varepsilon_n k_{z,n+1}} \tag{2}$$

$$R_n^{\mathrm{TE/TM}} = \frac{r_n^{\mathrm{TE/TM}} + R_{n+1}^{\mathrm{TE/TM}} e^{-j2k_{z,n+1}h_{n+1}}}{1 + R_{n+1}^{\mathrm{TE/TM}} r_n^{\mathrm{TE/TM}} e^{-j2k_{z,n+1}h_{n+1}}} \tag{3}$$

where $\perp$ represents the field component perpendicular to the incidence plane, $k_{z,n}$ is k_z in the nth layer and r_n^{TE} and r_n^{TM} are the local reflection coefficients of the nth layer for TE and TM polarization, respectively. R_n^{TE} and R_n^{TM} are the total reflection coefficients of the nth layer for TE and TM polarization, respectively. The local reflection coefficient of the nth layer is defined as the ratio of the reflected field to the incident field for a half-space medium consisting of the nth layer on top and the $(n+1)$th layer on the bottom. In contrast, the total reflection coefficient of the nth layer represents the complete ratio of the reflected field to the incident field, considering all layers stacked below the nth layer. The local reflection coefficient pertains to a single interface, whereas the total reflection coefficient is obtained recursively by accounting for the reflection coefficients of all underlying interfaces. The total PW reflection for TE/TM polarization at the PW reference plane is

$$\Gamma^{\mathrm{TE/TM}}(k_x, k_y) = R_0^{\mathrm{TE/TM}}(k_x, k_y)e^{-j2k_{z,0}h_0}. \tag{4}$$

For a multilayer medium ended with an unbounded subspace, the total reflection $R_N^{\mathrm{TE/TM}}$ equals $r_N^{\mathrm{TE/TM}}$. If the multilayer medium is ended to a perfect electric conductor (PEC) the total reflection coefficients $R_N^{\mathrm{TE}} = -1$ and $R_N^{\mathrm{TM}} = 1$ are used to start the calculation of the recursive equations (1)–(3).

B. Antenna Plane Wave Scattering Matrix

In Section II-A, we presented the analytical formulation for the response of an arbitrary multilayer medium to a known PW mode. Here, we provide a method for decomposing the radiated field of an arbitrary antenna into PW modes, as well as the antenna's response to different reflected PW modes.

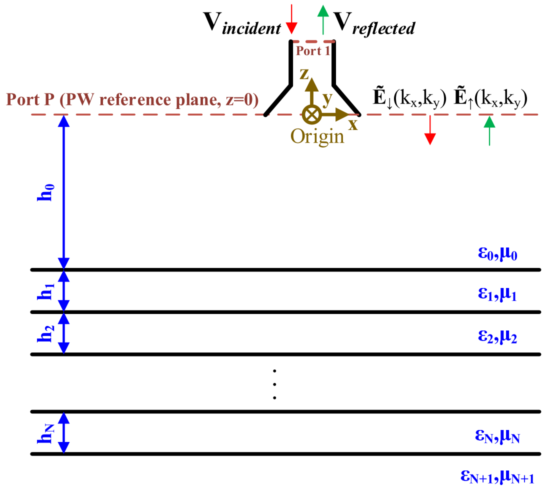

Fig. 1. Schematic of a radiating antenna in the presence of a multilayer medium.

The PWE of a known electric field E is the 2-D Fourier transform of the field that can be written as follows:

$$\tilde{\boldsymbol{E}}(k_x, k_y) = \int_{-\infty}^{\infty}\int_{-\infty}^{\infty} \boldsymbol{E}(x, y, z=0)e^{j(k_x x + k_y y)}dxdy. \quad (5)$$

Applying the wave equation to (5), the electric field $\boldsymbol{E}$ can be written as follows [39]:

$$\begin{aligned}\boldsymbol{E}&(x, y, z)\\ &= \frac{1}{4\pi^2}\Bigg[\int_{-\infty}^{\infty}\int_{-\infty}^{\infty} \tilde{\boldsymbol{E}}_\uparrow(k_x, k_y)e^{-j(k_x x+k_y y)}e^{-jk_z z}dk_x dk_y\\ &\quad + \int_{-\infty}^{\infty}\int_{-\infty}^{\infty} \tilde{\boldsymbol{E}}_\downarrow(k_x, k_y)e^{-j(k_x x+k_y y)}e^{+jk_z z}dk_x dk_y\Bigg]\end{aligned} \quad (6)$$

where $\tilde{\boldsymbol{E}}_\downarrow$ and $\tilde{\boldsymbol{E}}_\uparrow$ are the upward and downward propagating waves in the spectral domain. In (6), for $(k_x^2 + k_y^2)^{1/2} \le k$, the value of k_z is real; otherwise, it is imaginary. According to (6), in the first situation, the magnitude of the PW remains constant in a lossless medium, while in the second situation, the magnitude of the PW becomes evanescent as it moves away from $z = 0$. Therefore, for $(k_x^2 + k_y^2)^{1/2} \le k$, the PW modes are called propagating modes; otherwise, they are called evanescent modes. In this article, we ignore evanescent PWs. This approximation is applicable, when the antenna inductive fields are less than the radiating fields. The inductive fields can be neglected if the distance from the antenna is much greater than the wavelength. Ignoring evanescent PWs, the limits of the integration in (6) are restricted to a circle with the radius of k centered at the origin of the $k_x - k_y$ plane. In Fig. 1, the antenna places in $z > 0$, and the incident PWs propagate downward in $z < 0$.

The PWSM of an antenna introduced in [36] is an antenna model based on the PWE of the antenna radiated EM fields. In this model, we should consider a reference plane for the PWs. As depicted in Fig. 1, we consider $z = 0$ plane as the PWs reference plane. The PWSM of an antenna consists of four scattering parameters. These parameters include S_{11}, S_{P1}, S_{1P}, and S_{PP}. The first parameter is the well-known antenna free space reflection coefficient in the antenna theory [40]. The last parameter is the ratio of the PW reflected field from the antenna to the PW impinging on it. Here, we assume that we use an antenna for which the secondary-reflection from the antenna toward the $z < 0$ region is negligible. In such case, we can ignore S_{PP} in PWSM. Here, we focus on determining S_{P1} and S_{1P} of an antenna.

S_{P1} of PWSM is defined as follows [36]:

$$S_{P1}^{\mathrm{TE/TM}}(k_x, k_y) = \frac{\tilde{E}_\downarrow^{\mathrm{TE/TM}}(k_x, k_y)\Big|_{\text{in free space}}}{V_{\text{incident}}} \quad (7)$$

where V_{incident} is port 1 incident voltage and the measurement takes place in free space.

Ignoring the evanescent PWs in (6), the propagating PWs can be calculated using the far-field pattern of the antenna by using [39], [40]

$$\tilde{E}_\downarrow^{\mathrm{TE/TM}}(k_x, k_y) = \frac{-j2\pi r}{k_z e^{-jkr}} E_{\text{far-field}}^{\mathrm{TE/TM}}(\theta(k_x, k_y), \varphi(k_x, k_y)) \quad (8)$$

where $E_{\text{far-field}}$ is the complex far-field pattern of the electric field at the distance r from the origin. According to the definition of TE and TM polarizations, TE and TM components of the electric far-field are corresponding to $\hat{\boldsymbol{\phi}}$ and $\hat{\boldsymbol{\theta}}$, respectively. In (8), $\theta = \pi - \sin^{-1}((k_x^2 + k_y^2)^{1/2}/k_0)$ and $\varphi = \tan^{-1}(k_y/k_x)$ for $k_x > 0$ and $\varphi = \pi + \tan^{-1}(k_y/k_x)$ for $k_x < 0$. In order to calculate S_{P1}, we can calculate the far-field pattern of the desired antenna in the $z < 0$ hemisphere by 3-D EM simulation and using (7) and (8).

Based on the definition presented in [36], for an upward propagating PW given by $\boldsymbol{E_0}e^{-j(k_x x+k_y y+k_z z)}$, we introduce S_{1P} as follows:

$$S_{1P}^{\mathrm{TE/TM}}(k_x, k_y) = \frac{V_{\text{reflected}}}{E_0^{\mathrm{TE/TM}}}. \quad (9)$$

It should be noted that in contrast with ordinary scattering parameters, according to (7) and (9), the dimensions of S_{P1} and S_{1P} are $[m]$.

$S_{1P}^{\mathrm{TE/TM}}$ can be calculated using the reciprocity relation [36]

$$S_{1P}^{\mathrm{TE/TM}}(k_x, k_y) = \frac{-Z_0 k_z}{\eta_0 k} S_{P1}^{\mathrm{TE/TM}}(-k_x, -k_y) \quad (10)$$

where Z_0 is the characteristic impedance of the line connected to port 1 and η_0 is the characteristic impedance of the free space.

C. Antenna Reflection Coefficient in the Presence of a Multilayer Medium

Here, we combine the formulations presented in the two previous sections to derive a closed-form equation for calculating the reflection coefficient of an antenna in the presence of a multilayer medium. The total reflected voltage in port 1 is [36]

$$\begin{aligned}V_{\text{reflected}}&\\ = S_{11}&V_{\text{incident}}\\ &+ \frac{1}{4\pi^2}\int_{-k}^{k}\int_{-\sqrt{k^2-k_y^2}}^{\sqrt{k^2-k_y^2}} \tilde{E}_\uparrow^{\mathrm{TE}}(k_x, k_y)S_{1P}^{\mathrm{TE}}(k_x, k_y)dk_x dk_y\\ &+ \frac{1}{4\pi^2}\int_{-k}^{k}\int_{-\sqrt{k^2-k_y^2}}^{\sqrt{k^2-k_y^2}} \tilde{E}_\uparrow^{\mathrm{TM}}(k_x, k_y)S_{1P}^{\mathrm{TM}}(k_x, k_y)dk_x dk_y\end{aligned} \quad (11)$$

where S_{11} is the reflection coefficient of the antenna when placed in the free space. According to the definition of $\Gamma^{\mathrm{TE/TM}}$ in (4), the upward propagating spectral-domain electric field can be written as follows:

$$\tilde{E}_{\uparrow}^{\mathrm{TE}}(k_x, k_y) = -\Gamma^{\mathrm{TE}}(k_x, k_y)\tilde{E}_{\downarrow}^{\mathrm{TE}}(k_x, k_y) \tag{12}$$

and

$$\tilde{E}_{\uparrow}^{\mathrm{TM}}(k_x, k_y) = \Gamma^{\mathrm{TM}}(k_x, k_y)\tilde{E}_{\downarrow}^{\mathrm{TM}}(k_x, k_y). \tag{13}$$

Ignoring secondary reflections from the antenna, the total radiated PWs from the antenna can be written as follows:

$$\tilde{E}_{\downarrow}^{\mathrm{TE/TM}}(k_x, k_y) \simeq S_{P1}^{\mathrm{TE/TM}}(k_x, k_y)V_{\mathrm{incident}}. \tag{14}$$

Using (11)–(14), the reflection coefficient of the antenna in the presence of a multilayer medium can be written as follows:

$$\begin{aligned} S_{11,\mathrm{ML}} \simeq S_{11} &- \frac{1}{4\pi^2}\int_{-k}^{k}\int_{-\sqrt{k^2-k_y^2}}^{\sqrt{k^2-k_y^2}} \Gamma^{\mathrm{TE}}(k_x, k_y)S_{P1}^{\mathrm{TE}}(k_x, k_y) \\ &\times S_{1P}^{\mathrm{TE}}(k_x, k_y)dk_x dk_y \\ &+ \frac{1}{4\pi^2}\int_{-k}^{k}\int_{-\sqrt{k^2-k_y^2}}^{\sqrt{k^2-k_y^2}} \Gamma^{\mathrm{TM}}(k_x, k_y)S_{P1}^{\mathrm{TM}}(k_x, k_y) \\ &\times S_{1P}^{\mathrm{TM}}(k_x, k_y)dk_x dk_y. \end{aligned} \tag{15}$$

Compared with the full-wave radar equation [29], [31], there are two approximations in (15). The first approximation is due to ignoring the secondary reflections from the antenna-to-multilayer medium. The second one is due to ignoring the evanescent PWs.

D. Discretization Scheme

In order to calculate the integrals in (15), the k-space should be discretized. In the first step, we calculate $S_{P1}^{\mathrm{TE/TM}}$ using (7) and (8). In this work, we use a discretization scheme, in which the far-field points in (8) are selected in such a way that they are equally spaced in the $z < 0$ hemisphere of radius r in the far field of the antenna. In [41], the following approach is proposed to have M approximately equally spaced points in a hemisphere. In this scheme, all of the points are placed on m circles parallel to x–y plane, where m is given by

$$m = \left[\sqrt{\frac{M\pi}{8}}\right]. \tag{16}$$

Here, $[x]$ denotes the nearest integer to x. The θ angles corresponding to the points on these circles are

$$\theta_i = \pi - \left(i - \frac{1}{2}\right)\frac{\pi}{2m}, \quad i = 1, 2, \ldots, m \tag{17}$$

that select the $z < 0$ hemisphere. The number of points in each circle is given by

$$q_i = \begin{cases} \left[2M\sin(\theta_i)\sin\left(\dfrac{\pi}{4m}\right)\right], & \text{for } i = 1, 2, \ldots, m-1 \\ M - \displaystyle\sum_{l=i}^{m-1} q_l, & \text{for } i = m. \end{cases} \tag{18}$$

φ of the selected points are given by

$$\varphi_{ij} = \left(j - \frac{1}{2}\right)\left(\frac{2\pi}{q_i}\right), \quad j = 1, 2, \ldots, q_i. \tag{19}$$

In order to use the proposed discretization scheme to calculate the reflection coefficient of the antenna in the presence of a multilayered medium, we use the following substitution in (15) for an arbitrary integrand $g(k_x, k_y)$:

$$\begin{aligned} I &= \int_{-k}^{k}\int_{-\sqrt{k^2-k_y^2}}^{\sqrt{k^2-k_y^2}} g(k_x, k_y)dk_x dk_y \\ &= \int_{0}^{2\pi}\int_{0}^{k} g(k_\rho, \varphi)k_\rho dk_\rho d\varphi. \end{aligned} \tag{20}$$

Using the relation $k_\rho = k\sin\theta$, (20) can be written as follows:

$$\begin{aligned} I &= \int_{0}^{2\pi}\int_{\pi/2}^{\pi} g(\theta, \varphi)k^2\cos\theta\sin\theta d\theta d\varphi \\ &= \int_{\Omega_\downarrow} g(\theta, \varphi)k^2\cos\theta d\Omega \end{aligned} \tag{21}$$

where $d\Omega = \sin\theta d\theta d\varphi$ is the solid angle differential and $\Omega_\downarrow$ is the $z < 0$ hemisphere solid angle. The approximately equally spaced discretization scheme expressed by (17) and (19) results in approximately equal solid angles given by $\Delta\Omega \simeq 2\pi/M$. Hence, for large values of M, we can approximate the integral in (21) by

$$\begin{aligned} I &\simeq \sum_{i=1}^{m}\sum_{j=1}^{q_i} g(\theta_i, \varphi_{ij})k^2\cos\theta_i\Delta\Omega \\ &= \frac{2\pi k^2}{M}\sum_{i=1}^{m}\sum_{j=1}^{q_i} g(\theta_i, \varphi_{ij})\cos\theta_i. \end{aligned} \tag{22}$$

E. Fast Calculation of $S_{11,ML}$

The multilayer response to PW expressed by (1)–(4) depends only on the θ angle of the radiated PW and is independent of the φ angle. Therefore, $\Gamma^{\mathrm{TE/TM}}(k_x, k_y)$ in (15) can be expressed as $\Gamma^{\mathrm{TE/TM}}(\theta)$ for propagating PWs. Combining (22) and (15), the analytical reflection coefficient of an antenna placed over a multilayer medium can be expressed as follows:

$$\begin{aligned} S_{11,\mathrm{ML}} = S_{11} &- \frac{k^2}{2\pi M}\sum_{i=1}^{m}\sum_{j=1}^{q_i}\Gamma^{\mathrm{TE}}(\theta_i) \\ &\times S_{P1}^{\mathrm{TE}}(\theta_i, \varphi_{ij})S_{1P}^{\mathrm{TE}}(\theta_i, \varphi_{ij})\cos\theta_i \\ &+ \frac{k^2}{2\pi M}\sum_{i=1}^{m}\sum_{j=1}^{q_i}\Gamma^{\mathrm{TM}}(\theta_i)S_{P1}^{\mathrm{TM}}(\theta_i, \varphi_{ij}) \\ &\times S_{1P}^{\mathrm{TM}}(\theta_i, \varphi_{ij})\cos\theta_i. \end{aligned} \tag{23}$$

For simplicity, we introduce

$$T^{\mathrm{TE/TM}}(\theta_i) = \sum_{j=1}^{q_i} S_{P1}^{\mathrm{TE/TM}}(\theta_i, \varphi_{ij})S_{1P}^{\mathrm{TE/TM}}(\theta_i, \varphi_{ij})\cos\theta_i \tag{24}$$

and rewrite (23) as follows:

$$\begin{aligned} S_{11,\mathrm{ML}} = S_{11} + \frac{k^2}{2\pi M}\sum_{i=1}^{m}\big(&\Gamma^{\mathrm{TM}}(\theta_i)T^{\mathrm{TM}}(\theta_i) \\ &-\Gamma^{\mathrm{TE}}(\theta_i)T^{\mathrm{TE}}(\theta_i)\big). \end{aligned} \tag{25}$$

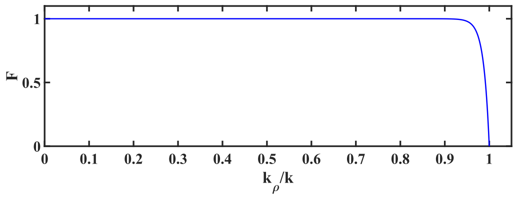

Fig. 2. k-space filter applied in calculation of $S_{11,\mathrm{ML}}$.

It should be noted that according to (16) the calculation time of $S_{11,\mathrm{ML}}$ in (25) is of the order of $\mathcal{O}(\sqrt{M})$.

F. Spectral Domain Filter

As discussed in Section II-B, we ignore the evanescent PWs in the proposed model and this causes a discontinuity in the $k_x - k_y$ plane at the boundary of $k_\rho = k_0$, where $k_\rho = k\sin\theta = (k_x^2 + k_y^2)^{1/2}$. This will cause an error in the modeled reflected signal. To suppress this effect, we apply a k-space filter defined as follows:

$$F = 1 - e^{-\gamma\left(1-\frac{k_\rho^2}{k^2}\right)}. \tag{26}$$

This equation is a hypothetical function to smooth the discontinuity in the k-space and has no physical meaning. In this equation, γ is a tuning parameter for the smoothness of the function. When γ increases, the function becomes smoother, but the accuracy of the PW expansion decreases. On the other hand, for low values of γ, the error due to discontinuity increases. For values of γ between 20 and 60, these errors do not differ meaningfully for the special antenna used in this article, and we set this parameter to 40. Fig. 2 illustrates the above spectral domain filter. Applying this filter, we can rewrite (25) as follows:

$$S_{11,\mathrm{ML}} = S_{11} + \frac{k^2}{2\pi M}\sum_{i=1}^{m}\Big(\big(\Gamma^{\mathrm{TM}}(\theta_i)T^{\mathrm{TM}}(\theta_i) - \Gamma^{\mathrm{TE}}(\theta_i)T^{\mathrm{TE}}(\theta_i)\big) \times F(\theta_i)\Big). \tag{27}$$

Fig. 3 depicts a summary of the actions needed for calculating the antenna reflection coefficient in the presence of a multilayer medium.

G. Theoretical Overview of the Existing Full-Wave Model

In order to compare our model with the existing full-wave models, we briefly explain these full-wave models. The main difference between the FFM and NFM presented by Lambot et al. [29], [31] is that they model antenna global reflection and transmission by single or multiple point sources, respectively. The FFM uses the monostatic spatial-domain Green's function that is calculated using

$$G_{ms} = \frac{1}{8\pi}\int_0^\infty \left(\frac{k_{z,0}R_0^{\mathrm{TM}}}{\omega\varepsilon} - \frac{\omega\mu R_0^{\mathrm{TE}}}{k_{z,0}}\right)e^{-j2k_{z,0}h_0}k_\rho dk_\rho \tag{28}$$

in which monostatic Green's function G_{ms} is the ratio of reflected electric field to the current of an infinitesimal dipole located at the same location [31], [33]. It should be noted that

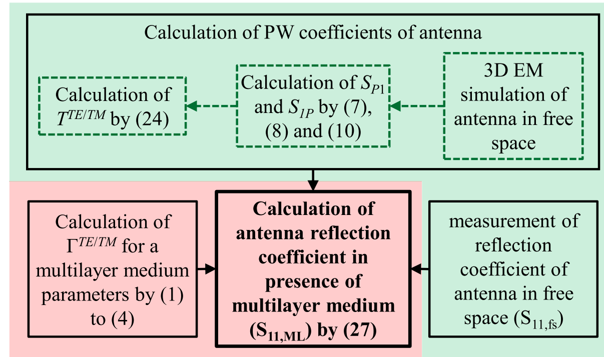

Fig. 3. Illustration of the calculation of $S_{11,\mathrm{ML}}$ as the forward problem solver for pavement thickness estimation. The blocks with a red background are executed once, while those with a green background are performed during each iteration of the optimization process.

according to (28), the evanescent modes are considered for point source response. The calculation of this integral is the main time-consuming process of the existing full-wave model. The NFM uses the bistatic spatial-domain Green's function expressed in [31] that is more time-consuming than the monostatic one. Furthermore, considering more point sources increases the number of bistatic spatial-domain Green's functions to be calculated. Therefore, the NFM is slower than the FFM. In this article, we compare the speed of our proposed model with the FFM.

In the FFM, there are three main parameters that characterize the antenna response. The first parameter is the antenna reflection coefficient in free space that we previously called it $S_{11,fs}$. the second parameter is H that is the product between the global transmission functions for the incident and backscattered fields. The third parameter is H_f that models the multiple reflections between the antenna and multilayer. H_f is actually the global reflection coefficient for the backscattered field. One can predict the reflection coefficient of the antenna in the presence of a known multilayer media using

$$S_{11,\mathrm{FFM}} = S_{11,fs} + \frac{HG_{ms}}{1 - H_f G_{ms}}. \tag{29}$$

There is another parameter that is not explicitly presented in (29), and it is the location of the point source with respect to antenna [42]. We use the same method as used in [29] to determine this parameter. The calculation of the multilayer structure spectral-domain Green's function is with respect to this location. In order to determine H and H_f for an antenna, we can measure the antenna reflection coefficient in the presence of a PEC at two known distances h_{pec1} and h_{pec2} and using the following equations [29]:

$$H_f = \frac{\frac{S_{11,pec2}-S_{11,fs}}{G_{ms,pec2}} - \frac{S_{11,pec1}-S_{11,fs}}{G_{ms,pec1}}}{S_{11,pec2} - S_{11,pec1}} \tag{30}$$

$$H = \frac{S_{11,pec2} - S_{11,fs}}{G_{ms,pec2}} - \left(S_{11,pec2} - S_{11,fs}\right)H_f. \tag{31}$$

In (30) and (31), $S_{11,\mathrm{pec1}}$ and $S_{11,\mathrm{pec2}}$ are the measured or, in our paper, simulated antenna reflection coefficient when the PEC is placed in distance of h_{pec1} and h_{pec2} from the point source location, respectively. Lambot et al. [43] have also used a more accurate approach that applies more different distances to overdetermine the system of equations. However, in this article, we use the approach formulated by (31) and (30). Only in far-field condition, the FFM parameters derived from (30) and (31) are independent of the distances of PEC from the point source location. However, if one calculates H and H_f by PECs placed in the near field of the antenna, as performed in [44], the FFM is valid when multilayer medium distance is near the distance used in PEC tests. Tran et al. [45] showed this modified FFM has sufficient accuracy for estimation of multilayer media unknowns when the antenna distance is more than $1.2D$, where D is the maximum dimension of antenna aperture.

H. Time-Domain Signals

In this article, we calculate the time-domain reflected signal from the frequency-domain GPR data. By using time-domain signal, we can apply time gating to neglect the unwanted part of signals in time. For this purpose, we first subtract the antenna reflection coefficient in free space from the antenna reflection coefficient in the presence of the multilayer medium. Next, we apply a windowing function in the frequency domain to decrease the ripple away from the main peaks of the time-domain signals. Here, we use the Tukey window [46]. This apodization window has a tuning parameter α to optimize the trade-off between low ripple level and maximum effective utilized bandwidth. For $\alpha = 0$, the window becomes rectangular and for $\alpha = 1$, it becomes a Hann window. We use $\alpha = 0.2$ empirically to achieve the best results in asphalt thickness estimation for a large dataset. The reflected signal in the time domain is defined as follows:

$$y(t) = \mathcal{F}^{-1}\left\{(S_{11,\mathrm{ML}}(f) - S_{11}(f))X(f)e^{-j2\pi f t_0}\right\} \quad (32)$$

where $\mathcal{F}^{-1}$ denotes the inverse Fourier transform and $X(f)$ is the Tukey window with $\alpha = 0.2$, as depicted in Fig. 4(a). The exponential term is used to make a time shift t_0 in the time-domain. In this article, we use the frequency data in the frequency range of 1–4 GHz that corresponds to the frequency bandwidth of $B = 3$ GHz. The inverse Fourier transform of $X(f)e^{-j2\pi f t_0}$, which is depicted in Fig. 4(b), can be interpreted as the time-domain incident signal.

I. Inversion

Up to this point, we proposed a method to calculate the reflected signal in the presence of a known multilayer medium. This method can be considered as a forward problem solver. The corresponding inverse problem is to estimate the medium parameters from a known reflected signal. We solve this inverse problem by using the particle swarm optimization (PSO) [47]. This method is a stochastic population-based optimization successfully applied in many function optimization problems and has fast convergence to acceptable solutions [48]. We use the following cost function:

$$C(\boldsymbol{\varepsilon}, \boldsymbol{h}) = \sum_i |y_{\mathrm{model}}(\boldsymbol{\varepsilon}, \boldsymbol{h}, t_i) - y_{\mathrm{measurement}}(t_i)|^2 \quad (33)$$

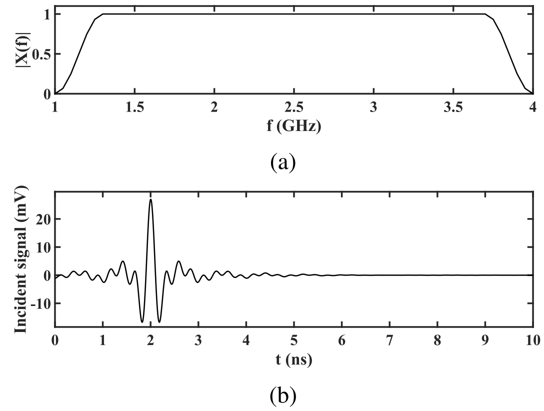

Fig. 4. (a) Absolute value of apodization window $X(f)$ and (b) its time-shifted inverse Fourier transform which can be assumed as a time-domain incident signal.

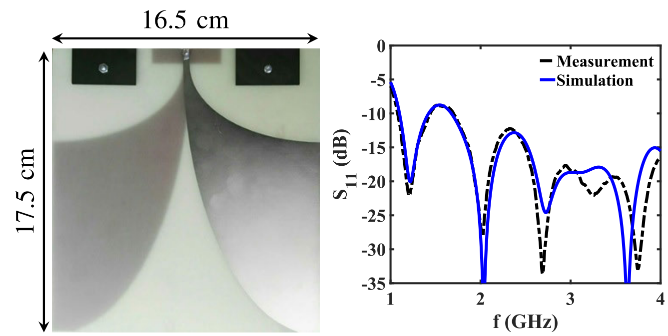

(a) (b)

Fig. 5. Antenna used for radiation in the presence of multilayer media. (a) Fabricated antenna and (b) free space reflection coefficient of the antenna.

where y_{model} denotes the reflected signal obtained by the proposed model and $y_{\mathrm{measurement}}$ is the reflected signal obtained from the measured data. Both y_{model} and $y_{\mathrm{measurement}}$ are calculated by using (32). $\boldsymbol{\varepsilon}$ and $\boldsymbol{h}$ are the vectors representing the complex electric permittivity and height of different layers of the medium. The optimized set of $(\boldsymbol{\varepsilon}_{\mathrm{opt}}, \boldsymbol{h}_{\mathrm{opt}})$, which corresponds to the minimum of the cost function, is considered as the estimated values for the medium parameters. In order to implement the PSO algorithm, we use the *particleswarm* function from MATLAB, with all parameters set to their default values, except for the function tolerance that we set it to 10^{-10}. This parameter determines the stopping criteria of the algorithm.

III. Model Implementation and Validation

In order to verify the validity of the proposed approach, we implement it for a Vivaldi antenna placed above an asphalt layer and compare the reflected signals obtained by the model with those obtained by 3-D full-wave electromagnetic simulation. In this section, we first explain the antenna used for simulations and measurements. Second, we discuss about the sufficient number of points, M, that discretize k-space. Finally, we compare the simulation results and the model results to verify the validity and accuracy of the model.

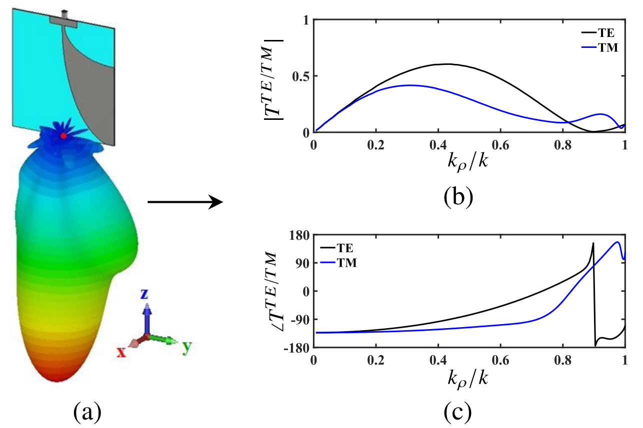

Fig. 6. (a) Magnitude of 3-D far-field pattern in the center frequency $f = 2.5$ GHz, (b) magnitude, and (c) phase of the extracted $T^{\mathrm{TE/TM}}$. The extraction process is repeated for all frequency steps. The phase of the far-field pattern depends on the origin of the far-field monitor that is shown in (a) by a red point. This point also serves as the phase reference for the PWs.

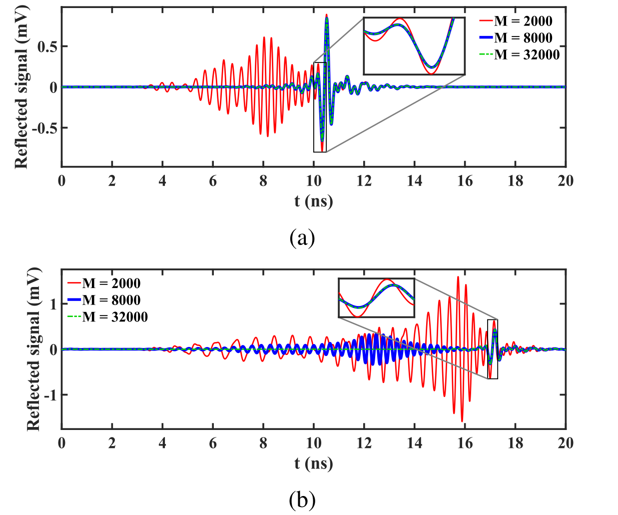

Fig. 7. Reflected signal calculated by the proposed model for an antenna radiating to a PEC surface placed at (a) $z = -1$ m and (b) $z = -2$ m.

A. Antenna

We used the Vivaldi antenna shown in Fig. 5(a) for thickness estimation of the asphalt layer. As represented in (27), the main parameters that should be extracted for the antenna in the proposed approach are $T^{\mathrm{TE/TM}}$ and antenna reflection coefficient in free space, S_{11}. In the optimization procedure used for thickness estimation, $T^{\mathrm{TE/TM}}$ is calculated only one time. We calculate this parameter by using the far-field radiation pattern of the 3-D EM simulation of the antenna in free space and applying (7), (8), (10), and (24). This process is shown in Fig. 6. The result of these simulation-based calculations is used in thickness estimation based on both simulated and measured data. $T^{\mathrm{TE/TM}}$ and S_{11} provide the complete information needed for modeling the antenna in the proposed method. The measurement and simulation results of the antenna reflection coefficient in free space, S_{11}, are depicted in Fig. 5(b). In this article, we obtain all 3-D EM simulation results by CST Microwave Studio software and perform all S_{11} measurements by an E8363b Agilent vector network analyzer.

B. Sufficient Number of Discretization Points

An important parameter that affects the calculation time is the number of discretization points, M. Fig. 7 shows the reflected signals from a PEC surface for three different values of M in two different situations. In the first situation, corresponding to Fig. 7(a), PEC is placed at $z = -1$ m, and in the second situation, corresponding to Fig. 7(b), PEC is placed at $z = -2$ m. As shown in Fig. 7, $M = 8000$ is sufficient for the first situation, and increasing M to 32 000 does not change the reflected signal, but in the second situation choosing $M = 8000$ leads to error. The reason for this phenomenon is that for scatterers placed far from the antenna, the phase difference between radiated PWs from neighboring discretization points is considerable, and to overcome this problem, M should be increased. To determine the proper value of M, the phase difference that occurred due to the two-way traveling time for the farthest scatterer should be considered. In this article, as the worst case, we consider a 10-cm thick asphalt layer with relative permittivity $\epsilon_{r1} = 9$ placed at 10-cm distance below the antenna aperture, and account for three multiple reflections. This case corresponds to 2-m two-way traveling of the PW in free space and in this condition $M = 8000$ is sufficient.

C. Verification and Comparison

We consider two problems to verify the validity of the proposed approach. In the first problem, the thickness of the asphalt layer is $h_1 = 7$ cm and echoes are nonoverlapped and in the second problem, the thickness of the asphalt layer is $h_1 = 1$ cm and echoes are overlapped. In both problems, the antenna is placed over an asphalt layer with $\epsilon_{r1} = 7$, and the distance between the antenna aperture to the asphalt layer is $h_0 = 10$ cm. Note that, in the simulation scenarios, the two-way distance of the multilayer from the antenna is greater but not much greater than the wavelength. Therefore, neglecting evanescent PWs can introduce some errors and should be investigated. We use CST microwave software to calculate the reflection coefficient of the antenna in free space and also in the presence of the asphalt layer and then use (32) to calculate the reflected signal as the reference. In this full-wave simulation, all EM phenomena are considered including the secondary reflection from the antenna. However, the drawback of using this simulation in solving the inverse problem is its low calculation speed. The simulation of the antenna in the presence of the asphalt layer takes about 6 h using an Intel[1] core[2] i7-2600k CPU with 3.4-GHz clock rate. In order to compare our proposed model with the FFM, here, we implement the FFM model. The location of a point source is 6.5 cm above the antenna aperture using the method declared in [29]. The distances of PEC in two tests used in (30) and (31) are 9 and 11 cm. Fig. 8(a) and (b) depicts the reflected signals obtained by the full-wave simulation, the proposed approach

[1]Registered Trademark.
[2]Trademarked.

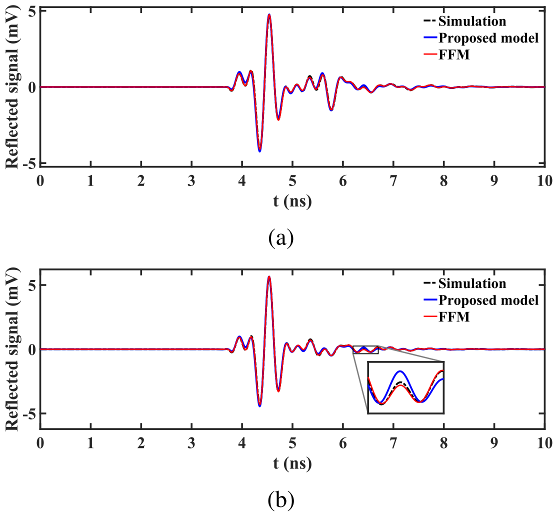

Fig. 8. Comparison of reflected signals obtained by the proposed approach, FFM and the 3-D electromagnetic simulation for the two cases of (a) nonoverlapped echoes and (b) overlapped echoes. We applied a smooth time gating for $t < 4$ ns.

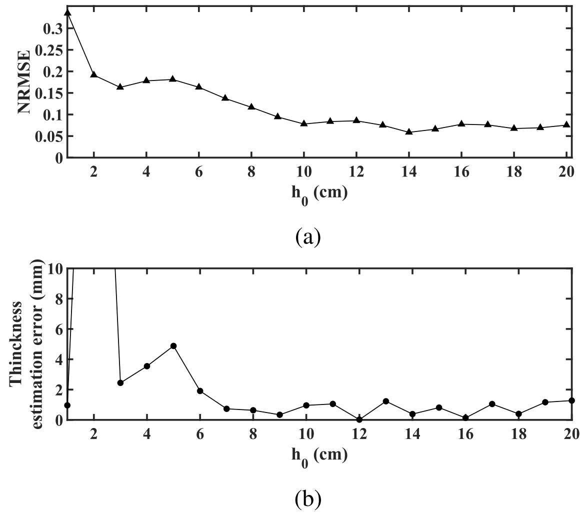

Fig. 9. (a) NRMSE of forward problem solver and (b) consequent error in thickness estimation as a function of antenna-to-multilayer distance, obtained for $h_1 = 1$ cm, $\epsilon_{r1} = 6$, $\epsilon_{r2} = 4$, and $\sigma_1 = 0.04$ S/m.

TABLE I

NRMSE and Calculation Time of the Proposed Approach and FFM for Two Cases With Nonoverlaped Echoes ($h_1 = 7$ cm) and Overlapped Echoes ($h_1 = 1$ cm)

h_1 (cm)	NRMSE		calculation time (ms)	
	FFM	proposed model	FFM	proposed model
1	0.028	0.077	69 ± 2	0.60 ± 0.02
7	0.035	0.099	68 ± 2	0.58 ± 0.02

and the FFM for the first and second problems, respectively. In both problems, there is a good agreement between the proposed approach, FFM, and simulation. In order to compare the accuracy of the models, we use normalized root mean square error (NRMSE) defined by

$$\mathrm{NRMSE} = \sqrt{\frac{\sum_{i=1}^{N_t} |y_{\mathrm{model}}(t_i) - y_{\mathrm{CST}}(t_i)|^2}{\sum_{i=1}^{N_t} |y_{\mathrm{CST}}(t_i)|^2}} \tag{34}$$

where N_t is the number of time steps in the time-domain signal, y_{CST} is the reflected signal obtained by CST, and y_{model} is the reflected signal obtained either by the FFM or proposed approach. Table I presents the comparison of NRMSE and calculation time. The accuracy of the FFM is more than the proposed method; however, the results show more than 100 times speed improvement in the proposed approach compared with the FFM. The reported calculation time for the proposed modeling approach also includes the IFFT time with 2001 points.

IV. Asphalt Thickness Estimation Results

In the problem of asphalt thickness estimation, the asphalt thickness and permittivity are unknown. As pointed out before, the PSO optimization algorithm and the proposed antenna model are used to estimate the asphalt thickness. To model more realistic multilayer parameters, we take into account that the first layer is lossy. The lossy material electric permittivity is represented as $\epsilon_1 = \epsilon_{r1}\epsilon_0 - j(\sigma_1/\omega)$, where ϵ_{r1} and σ_1 are the real part of relative permittivity and conductivity of the first layer, respectively. In the optimization process, we use a time gating for $t > 4$ ns to eliminate the remaining errors after subtraction of the antenna free space reflection coefficient. In the following, we present the thickness estimation results. In Section IV-A, we study the effect of antenna-to-multilayer distance on the thickness estimation error using simulated data. In Section IV-B, we investigate the accuracy of asphalt thickness estimation for different values of asphalt thickness and permittivity. In Sections IV-A and IV-B, to evaluate $y_{\mathrm{measurement}}$ in (33), we use the CST Microwave simulation results instead of the measurement results. In Section IV-D, for an asphalt layer and three PVC layers with different thicknesses, S_{11} and $S_{11,\mathrm{ML}}$ are used to evaluate $y_{\mathrm{measurement}}$ in (33) and then PSO algorithm is applied to estimate the asphalt layer thickness.

A. Effect of Antenna-to-Multilayer Distance on Thickness Estimation Error

Our proposed approach relies on two approximations, namely, ignoring evanescent PWs and antenna–medium interactions from the antenna. The effect of these approximations is reduced by increasing the distance between the antenna and multilayered medium. Here, we study the impact of the antenna-to-multilayer distance on the model error and the consequent estimation error of layer thickness. For this purpose, we conduct full-wave simulations for an overlapped-echoes scenario, considering the following multilayer parameters: $h_1 = 1$ cm, $\epsilon_{r1} = 6$, $\epsilon_{r2} = 4$, and $\sigma_1 = 0.04$ S/m. In Fig. 9(a) and (b), for different values of h_0, the NRMSE between the modeled and full-wave simulated reflected signals and the thickness estimation error are presented, respectively. Our results indicate that the thickness estimation error remains below 1.5 mm when the NRMSE is below 0.1. Consequently, we can state that for h_0 values of 10 cm or greater, the thickness estimation error is within acceptable limits for this particular example. These results may vary depending on the particular model configuration, determining parameter sensitivities.

TABLE II

ESTIMATED THICKNESS h_{est} FOR DIFFERENT THICKNESSES AND ELECTRIC PERMITTIVITIES, OBTAINED FOR $h_0 = 15$ cm, $\epsilon_{r2} = 4$, AND $\sigma_1 = 0.04$ S/m

ϵ_{r1}	h_1 = 1 cm		h_1 = 4 cm		h_1 = 7 cm	
	$B\Delta\tau$	h_{est} (cm)	$B\Delta\tau$	h_{est} (cm)	$B\Delta\tau$	h_{est} (cm)
2	0.28	1.09	1.13	4.20	1.98	7.19
6	0.49	1.08	1.96	4.05	3.43	7.12
9	0.60	1.09	2.40	4.18	4.20	7.26

TABLE III

EFFECT OF ADDING NOISE ON THE THICKNESS ESTIMATION ERROR FOR $h_0 = 15$ cm, $h_1 = 1$ cm, $\sigma_1 = 0.04$ S/m, AND $\epsilon_{r2} = 4$

SNR (dB)	Error < 2 mm (%)		
	$\epsilon_{r1} = 2$	$\epsilon_{r1} = 6$	$\epsilon_{r1} = 9$
30	64	20	88
40	94	96	100
50	100	100	100

B. Estimation Accuracy for Different Layer Parameters

We simulate the reflection coefficient of the antenna placed above an asphalt layer with relative permittivity of $\epsilon_{r1} = [2, 6, 9]$, conductivity of $\sigma_1 = 0.04$ S/m, and thickness of $h_1 = [1, 4, 7]$ cm. The distance of antenna aperture from the multilayer is $h_0 = 15$ cm. Thickness of the asphalt sublayer is considered to be infinite, and its relative permittivity is set equal to 4. We used the result of these simulations as the measurement data in the cost function defined in (33). In the inverse problem, there are four unknowns, namely, the thickness, permittivity, and conductivity of the first layer and permittivity of the second layer. The estimated values of thickness in these situations are expressed in Table II. It can be seen that the proposed model is effective for both cases that $B\Delta\tau$ is greater or less than 1, and this confirms the super-resolution capability of the method. The maximum error of asphalt thickness estimation in Table II is 2.6 mm. Because of the random nature of the PSO algorithm, the thickness estimation calculation time cannot be expressed precisely; however, we can report that it ranges from 4 to 8 s.

C. Effect of Noise on Thickness Estimation Error

To investigate the impact of noise on the super-resolution capability of the method, we introduce numerical noise to simulated data. Following a similar approach to [26], we define the signal-to-noise ratio (SNR) as the ratio between the power of the strongest echo in the time domain and the variance of the noise. We added random Gaussian noise with an average of zero to simulated S_{11} data. Considering the stochastic nature of noise, this procedure is repeated 50 times. Table III presents the results of thickness estimation error for three overlapped-echo scenarios with the following parameters: $h_0 = 15$ cm, $\epsilon_{r1} = [2, 6, 9]$, $h_1 = 1$ cm, $\sigma_1 = 0.04$ S/m, and $\epsilon_{r2} = 4$. We consider three different SNR values. For SNR values greater than 40 dB, at least 94% of samples have a thickness estimation error of less than 2 mm. Achieving an SNR of 40 dB in the time domain is equivalent to adding Gaussian noise with variances of -46.9, -42.3, and -40.4 dB to the S_{11} data in the frequency domain for three scenarios with ϵ_{r1} of 2, 6, and 9, respectively. In practice, the measurement system noise level remains below these values. However, the main source of error typically arises from non-Gaussian noise, which is difficult to quantify as it depends on many factors, including the radar.

D. Thickness Estimation Based on Measurement Data

In the proposed approach, we used the 3-D full-wave simulated data to model the antenna and obviously, there is some differences between the simulated and the fabricated antenna. Therefore, it is important to verify the validity of this modeling approach using measured data. A difference between the simulated and measured data is the time mismatch between the location of the port in the 3-D simulation and the point the VNA calibration performed. In order to find this mismatch, we used a test in which we place a PEC plate at a measured distance from antenna aperture. Then, we used the reflected signal of this measurement in comparison with the proposed approach reflected signal to determine the time difference. Using this calibration process, we calculated a 64-ps time difference and applied it as a time shift to all measured data. Here, we use two sets of measurements—one with asphalt layer and another with PVC layer.

As depicted in Fig. 10(a), the measurement setup consists of an asphalt layer placed on a PEC plate. This layer consists of two asphalt slabs of dimensions 39 $\times$ 29 $\times$ 5 cm placed next together. These dimensions does not meet the multilayer independence in the horizontal direction. In order to partially overcome this problem, we performed 30 measurements with random displacement of the asphalt layer in the horizontal direction. In these measurements, the edge effects differ randomly while the thickness remains constant. Then, we use the average S_{11} of the tests as the measured data. This averaging also decreases the effect of the gap between asphalt slabs. The PEC plate material is aluminum. The distance between the lower edge of the antenna and the asphalt layer is 15.6 cm. Using the PSO optimization algorithm, we achieved the values of $h_1 = 5.19$ cm, $\epsilon_{r1} = 6.1$, and $\sigma_1 = 0.06$ S/m. Fig. 10(b) shows the measured reflected signal and the signal provided by the proposed approach for the estimated values of the multilayer parameters. As can be seen from Fig. 10(b), there are three reflected echoes in the range of 4.5–7 ns. The first and second echoes correspond to the reflection from the asphalt top surface and the PEC surface, respectively. The third echo is due to the multiple reflections in the asphalt layer. As discussed in Section III-A, the calculation of $T^{\text{TE/TM}}$ is based on a 3-D electromagnetic simulation of the designed antenna, which inherently have practical mismatches with the fabricated antenna. According to Fig. 10(b), at least in the context of calculating $T^{\text{TE/TM}}$, the mismatch can be considered negligible. In order to see the cost function in a global search, we plotted it in Fig. 10(c). To plot this figure, we used the estimated conductivity $\sigma_1 = 0.06$ S/m. Based on the inset of Fig. 10(c), there exists a narrow strip where the cost function approaches its minimum value. Considering the length of this narrow strip, even a slight discrepancy between the modeled and exact reflection coefficient can lead to an estimated thickness error of approximately 2 mm.

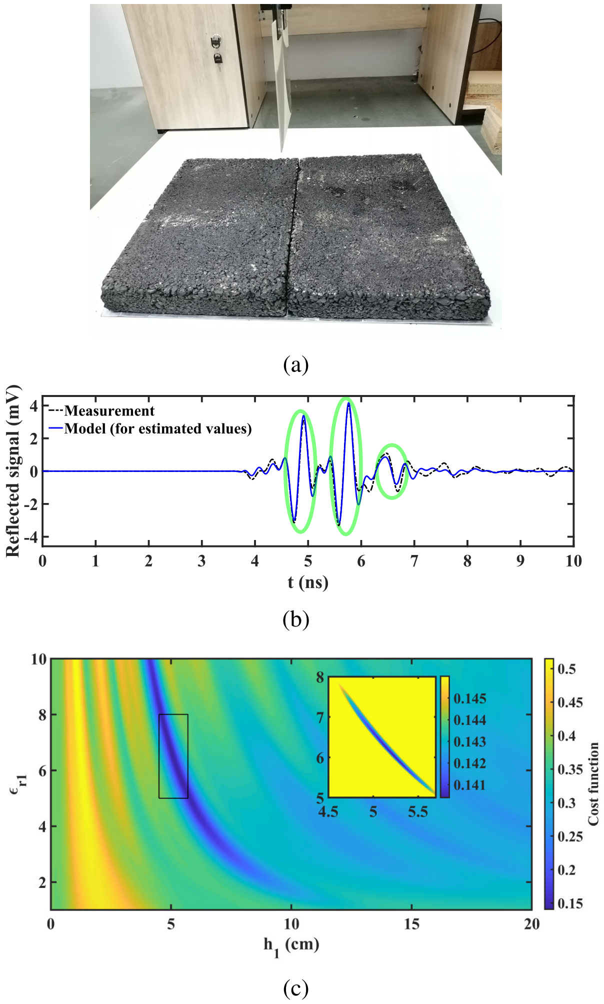

Fig. 10. (a) Measurement setup that consists of an asphalt layer placed on a PEC plate and (b) comparison of the reflected signal obtained by the proposed model for the estimated values of the multilayer parameters and measured reflected signal. We applied a smooth time gating for $t < 4$ ns. The first three echoes, highlighted by green ovals, represent the reflection from the asphalt's top layer, the reflection from the metal plate, and the secondary reflection occurring within the asphalt layer, respectively. (c) Cost function for $\sigma_1 = 0.06$ S/m in terms of thickness and permittivity. In order to have better insight, we applied a threshold of 0.146 to the values in the inset.

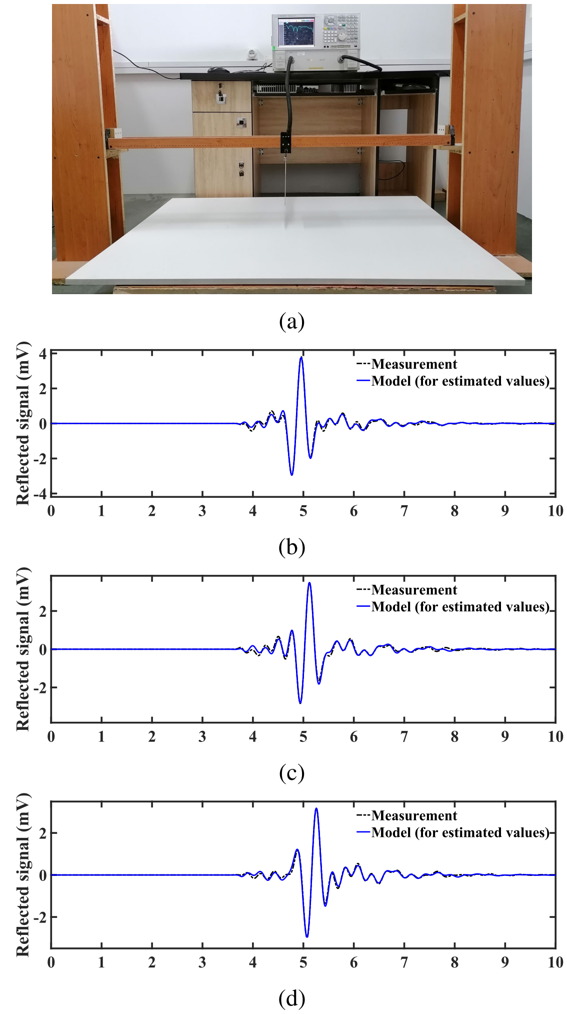

Fig. 11. (a) Measurement setup that consists of a PVC slab placed on a PEC plate and (b) comparison of the reflected signal obtained by the proposed model for the estimated values for a single PVC slab ($h_1 = 1.6$ cm). (c) Two PVC slabs ($h_1 = 3.2$ cm) and (d) three PVC slabs ($h_1 = 4.8$ cm). We applied a smooth time gating for $t < 4$ ns.

In order to validate the modeling approach by more challenging measurements, we used PVC slabs with a thickness of 1.6 cm and horizontal dimension of 1.22 × 0.9 m. To have a more complete set of measurements we use single, double, and triple slabs placed on a PEC plate. Fig. 11(a) depicts the measurement setup for a single PVC test. The distance of the PVC layer from the antenna aperture in all of the PVC measurements is 14.4 cm. The permittivity of PVC is about 2 and the corresponding $B\Delta\tau$ is about 0.45, 0.9, and 1.35, respectively. The two first measurements meet the super-resolution condition. The estimated PVC thickness for the tests is 1.78, 3.43, and 4.67 cm, respectively. Fig. 11(b)–(d) shows the modeled outputs using estimated values of the layer and the measured outputs for the three tests, respectively.

V. Conclusion

In our study, we presented the formulation of the antenna reflection coefficient in the presence of multilayer media by omitting considerations of evanescent waves and interactions between the antenna and the medium, whose impacts diminish as the antenna height increases. Furthermore, we formulated the antenna model within the spectral domain, enabling the explicit incorporation of the antenna's frequency-dependent radiation pattern. Our aim is to offer a faster calculation approach that broadens the scope of full-wave inversion techniques, while ensuring that modeling inaccuracies remain minimal. The calculation speed of this approach is about 100 times faster than the model used in [29]. We verified the validity of this approach by comparing the reflected signal calculated by the model and that obtained by 3-D full-wave simulation. We performed this verification for a problem that the multilayer medium was placed at 10-cm distance from the antenna aperture. In this paper, we used the proposed modeling approach in companion with the PSO optimization algorithm in the practical problem of asphalt thickness estimation. Based on simulation data, we confirmed the super-resolution capability of this method for thickness estimation. We also applied measurement data for an asphalt layer and a thin PVC layer placed over a PEC plate. According to the estimation results based on simulation and measurements, for the situations that the echoes are overlapped and the antenna distance from the multilayer is about 15 cm, the absolute error is about 2 mm.

REFERENCES

[1] S. Zhao and I. L. Al-Qadi, "Super-resolution of 3-D GPR signals to estimate thin asphalt overlay thickness using the XCMP method," *IEEE Trans. Geosci. Remote Sens.*, vol. 57, no. 2, pp. 893–901, Feb. 2019.

[2] H. Liu and M. Sato, "In situ measurement of pavement thickness and dielectric permittivity by GPR using an antenna array," *NDT & E Int.*, vol. 64, pp. 65–71, Jun. 2014.

[3] A. Loizos and C. Plati, "Accuracy of ground penetrating radar horn-antenna technique for sensing pavement subsurface," *IEEE Sensors J.*, vol. 7, no. 5, pp. 842–850, May 2007.

[4] S. Wang, S. Zhao, and I. L. Al-Qadi, "Continuous real-time monitoring of flexible pavement layer density and thickness using ground penetrating radar," *NDT & E Int.*, vol. 100, pp. 48–54, Dec. 2018.

[5] K. Grote, S. Hubbard, J. Harvey, and Y. Rubin, "Evaluation of infiltration in layered pavements using surface GPR reflection techniques," *J. Appl. Geophys.*, vol. 57, no. 2, pp. 129–153, Feb. 2005.

[6] F. M. Fernandes, A. Fernandes, and J. Pais, "Assessment of the density and moisture content of asphalt mixtures of road pavements," *Construct. Building Mater.*, vol. 154, pp. 1216–1225, Nov. 2017.

[7] J. Minet, P. Bogaert, M. Vanclooster, and S. Lambot, "Validation of ground penetrating radar full-waveform inversion for field scale soil moisture mapping," *J. Hydrol.*, vols. 424–425, pp. 112–123, Mar. 2012.

[8] L. Yi, L. Zou, K. Takahashi, and M. Sato, "High-resolution velocity analysis method using the ℓ-1 norm regularized least-squares method for pavement inspection," *IEEE J. Sel. Topics Appl. Earth Observ. Remote Sens.*, vol. 11, no. 3, pp. 1005–1015, Jan. 2018.

[9] S. Wang, S. Zhao, and I. L. Al-Qadi, "Real-time monitoring of asphalt concrete pavement density during construction using ground penetrating radar: Theory to practice," *Transp. Res. Rec., J. Transp. Res. Board*, vol. 2673, no. 5, pp. 329–338, May 2019.

[10] I. L. Al-Qadi, Z. Leng, S. Lahouar, and J. Baek, "In-place hot-mix asphalt density estimation using ground-penetrating radar," *Transp. Res. Rec., J. Transp. Res. Board*, vol. 2152, no. 1, pp. 19–27, Jan. 2010.

[11] S. Zhao, "Development of GPR data analysis algorithms for predicting thin asphalt concrete overlay thickness and density," Ph.D. dissertation, Dept. Civil Environ. Eng., Univ. Illinois Urbana-Champaign, Champaign, IL, USA, 2018.

[12] A. De Coster, A. Van der Wielen, C. Grégoire, and S. Lambot, "Evaluation of pavement layer thicknesses using GPR: A comparison between full-wave inversion and the straight-ray method," *Construct. Building Mater.*, vol. 168, pp. 91–104, Apr. 2018.

[13] L. Edwards and H. P. Bell, "Comparative evaluation of nondestructive devices for measuring pavement thickness in the field," *Int. J. Pavement Res. Technol.*, vol. 9, no. 2, pp. 102–111, Mar. 2016.

[14] S. B. Thomas and L. P. Roy, "Impact of GPR antenna height in estimating coal layer thickness using spatial smoothing techniques," *IET Sci., Meas. Technol.*, vol. 14, no. 10, pp. 906–912, Dec. 2020.

[15] J. Minet, A. Wahyudi, P. Bogaert, M. Vanclooster, and S. Lambot, "Mapping shallow soil moisture profiles at the field scale using full-waveform inversion of ground penetrating radar data," *Geoderma*, vol. 161, nos. 3–4, pp. 225–237, Mar. 2011.

[16] I. L. Al-Qadi, S. Lahouar, and A. Loulizi, "Successful application of ground-penetrating radar for quality assurance-quality control of new pavements," *Transp. Res. Rec., J. Transp. Res. Board*, vol. 1861, no. 1, pp. 86–97, Jan. 2003.

[17] S. Zhao and I. L. Al-Qadi, "Development of an analytic approach utilizing the extended common midpoint method to estimate asphalt pavement thickness with 3-D ground-penetrating radar," *NDT & E Int.*, vol. 78, pp. 29–36, Mar. 2016.

[18] C. Plati and A. Loizos, "Using ground-penetrating radar for assessing the structural needs of asphalt pavements," *Nondestruct. Test. Eval.*, vol. 27, no. 3, pp. 273–284, Sep. 2012.

[19] S. Lahouar, I. L. Al-Qadi, A. Loulizi, T. M. Clark, and D. T. Lee, "Approach to determining in situ dielectric constant of pavements: Development and implementation at interstate 81 in Virginia," *Transp. Res. Rec., J. Transp. Res. Board*, vol. 1806, no. 1, pp. 81–87, Jan. 2002.

[20] J. De Pue, M. Van Meirvenne, and W. M. Cornelis, "Accounting for surface refraction in velocity semblance analysis with air-coupled GPR," *IEEE J. Sel. Topics Appl. Earth Observ. Remote Sens.*, vol. 9, no. 1, pp. 60–73, Jan. 2016.

[21] Z. Leng and I. L. Al-Qadi, "An innovative method for measuring pavement dielectric constant using the extended CMP method with two air-coupled GPR systems," *NDT & E Int.*, vol. 66, pp. 90–98, Sep. 2014.

[22] C. Le Bastard, V. Baltazart, Y. Wang, and J. Saillard, "Thin-pavement thickness estimation using GPR with high-resolution and superresolution methods," *IEEE Trans. Geosci. Remote Sens.*, vol. 45, no. 8, pp. 2511–2519, Aug. 2007.

[23] U. Spagnolini, "Permittivity measurements of multilayered media with monostatic pulse radar," *IEEE Trans. Geosci. Remote Sens.*, vol. 35, no. 2, pp. 454–463, Mar. 1997.

[24] S. Zhao and I. L. Al-Qadi, "Development of regularization methods on simulated ground-penetrating radar signals to predict thin asphalt overlay thickness," *Signal Process.*, vol. 132, pp. 261–271, Mar. 2017.

[25] S. Zhao, P. Shangguan, and I. L. Al-Qadi, "Application of regularized deconvolution technique for predicting pavement thin layer thicknesses from ground penetrating radar data," *NDT & E Int.*, vol. 73, pp. 1–7, Jul. 2015.

[26] C. Le Bastard, Y. Wang, V. Baltazart, and X. Dérobert, "Time delay and permittivity estimation by ground-penetrating radar with support vector regression," *IEEE Geosci. Remote Sens. Lett.*, vol. 11, no. 4, pp. 873–877, Apr. 2014.

[27] C. Patriarca, S. Lambot, M. R. Mahmoudzadeh, J. Minet, and E. Slob, "Reconstruction of sub-wavelength fractures and physical properties of masonry media using full-waveform inversion of proximal penetrating radar," *J. Appl. Geophys.*, vol. 74, no. 1, pp. 26–37, May 2011.

[28] J. Minet, S. Lambot, E. C. Slob, and M. Vanclooster, "Soil surface water content estimation by full-waveform GPR signal inversion in the presence of thin layers," *IEEE Trans. Geosci. Remote Sens.*, vol. 48, no. 3, pp. 1138–1150, Mar. 2010.

[29] S. Lambot, E. C. Slob, I. van den Bosch, B. Stockbroeckx, and M. Vanclooster, "Modeling of ground-penetrating radar for accurate characterization of subsurface electric properties," *IEEE Trans. Geosci. Remote Sens.*, vol. 42, no. 11, pp. 2555–2568, Nov. 2004.

[30] S. Lambot, E. C. Slob, I. van den Bosch, B. Stockbroeckx, B. Scheers, and M. Vanclooster, "Estimating soil electric properties from monostatic ground-penetrating radar signal inversion in the frequency domain," *Water Resour. Res.*, vol. 40, no. 4, pp. 1–12, Apr. 2004.

[31] S. Lambot and F. André, "Full-wave modeling of near-field radar data for planar layered media reconstruction," *IEEE Trans. Geosci. Remote Sens.*, vol. 52, no. 5, pp. 2295–2303, May 2014.

[32] K. Z. Jadoon, S. Lambot, B. Scharnagl, J. van der Kruk, E. Slob, and H. Vereecken, "Quantifying field-scale surface soil water content from proximal GPR signal inversion in the time domain," *Near Surf. Geophys.*, vol. 8, no. 6, pp. 483–491, Dec. 2010.

[33] S. Lambot, E. Slob, and H. Vereecken, "Fast evaluation of zero-offset Green's function for layered media with application to ground-penetrating radar," *Geophys. Res. Lett.*, vol. 34, no. 21, pp. 1–6, Nov. 2007.

[34] M. Ayatollahi and S. Safavi-Naeini, "A new representation for the Green's function of multilayer media based on plane wave expansion," *IEEE Trans. Antennas Propag.*, vol. 52, no. 6, pp. 1548–1557, Jun. 2004.

[35] K. Wu, H. Desesquelles, R. Cockenpot, L. Guyard, V. Cuisiniez, and S. Lambot, "Ground-penetrating radar full-wave inversion for soil moisture mapping in trench-hill potato fields for precise irrigation," *Remote Sens.*, vol. 14, no. 23, p. 6046, Nov. 2022.

[36] D. M. Kerns, *Plane-Wave Scattering-Matrix Theory of Antennas and Antenna-Antenna Interactions*, vol. 162. Gaithersburg, MD, USA: National Bureau of Standards, Department of Commerce, 1981.

[37] C. A. Balanis, *Advanced Engineering Electromagnetics*. Hoboken, NJ, USA: Wiley, 2012.

[38] W. C. Chew, *Waves and Fields in Inhomogenous Media*. Hoboken, NJ, USA: Wiley, 1999.

[39] S. Gregson, J. McCormick, and C. Parini, *Principles of Planar Near-Field Antenna Measurements*, vol. 53. Edison, NJ, USA: IET, 2007.

[40] C. A. Balanis, *Antenna Theory: Analysis Design*. Hoboken, NJ, USA: Wiley, 2016.

[41] C. G. Koay, "A simple scheme for generating nearly uniform distribution of antipodally symmetric points on the unit sphere," *J. Comput. Sci.*, vol. 2, no. 4, pp. 377–381, Dec. 2011.

[42] K. Z. Jadoon, S. Lambot, E. C. Slob, and H. Vereecken, "Analysis of horn antenna transfer functions and phase-center position for modeling off-ground GPR," *IEEE Trans. Geosci. Remote Sens.*, vol. 49, no. 5, pp. 1649–1662, May 2011.

[43] S. Lambot, M. Antoine, M. Vanclooster, and E. C. Slob, "Effect of soil roughness on the inversion of off-ground monostatic GPR signal for noninvasive quantification of soil properties," *Water Resour. Res.*, vol. 42, no. 3, pp. 1–10, Mar. 2006.

[44] A. Ihamouten et al., "Full-waveform inversion using a stepped-frequency GPR to characterize the tack coat in hot-mix asphalt (HMA) layers of flexible pavements," *NDT & E Int.*, vol. 95, pp. 17–25, Apr. 2018.

[45] A. P. Tran, F. André, C. Craeye, and S. Lambot, "Near-field or far-field full-wave ground penetrating radar modeling as a function of the antenna height above a planar layered medium," *Prog. Electromagn. Res.*, vol. 141, pp. 415–430, 2013.

[46] P. Bloomfield, *Fourier Analysis of Time Series: An Introduction*. Hoboken, NJ, USA: Wiley, 2004.

[47] M. Clerc, *Particle Swarm Optimization*, vol. 93. Hoboken, NJ, USA: Wiley, 2010.

[48] M. R. Bonyadi and Z. Michalewicz, "Particle swarm optimization for single objective continuous space problems: A review," *Evol. Comput.*, vol. 25, no. 1, pp. 1–54, Mar. 2017.

Ramin Roohi received the B.S. degree in electrical engineering from the Ferdowsi University of Mashhad, Mashhad, Iran, in 2012, and the M.S. degree in electrical engineering from Tarbiat Modares University, Tehran, Iran, in 2015. He is currently pursuing the Ph.D. degree with the Ferdowsi University of Mashhad.

His research interests include plane wave expansion, antenna modeling, and ground-penetrating radar.

Amir Reza Attari was born in Mashhad, Iran, in 1971. He received the B.S. and M.S. degrees in electrical engineering from the Sharif University of Technology, Tehran, Iran, in 1994 and 1996, respectively, and the joint Ph.D. degree in electrical engineering from the Sharif University of Technology, and the University Joseph Fourier, Grenoble, France, in 2002.

In 2004, he joined the Department of Electrical Engineering, Ferdowsi University of Mashhad, Mashhad, where he is currently a Professor. His research interests include antennas, passive microwave devices, and microwave imaging.

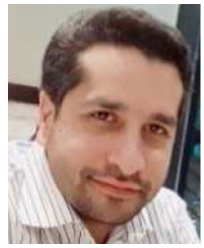

Mohammad Saeed Majedi was born in Shiraz, Iran, in 1983. He received the B.S. degree in electrical engineering from the Ferdowsi University of Mashhad, Mashhad, Iran, in 2006, the M.S. degree in electrical engineering from the Sharif University of Technology, Tehran, Iran, in 2008, and the Ph.D. degree in electrical engineering from the Ferdowsi University of Mashhad in 2013.

In 2013, he joined the Department of Electrical Engineering, Ferdowsi University of Mashhad, where he is currently an Associate Professor. His research interests include antenna, microwave circuits, and microwave imaging.

Sébastien Lambot (Member, IEEE) received the M.Sc. and Ph.D. degrees in agricultural and environmental engineering from the Université catholique de Louvain (UCLouvain), Louvain-la-Neuve, Belgium, in 1999 and 2003, respectively.

From 2006 to 2012, he held joint appointments at UCLouvain, where he was appointed as a Professor, and Forschungszentrum Jülich, Jülich, Germany, where he served as a Research Group Leader. He is currently a Full-Professor (part-time) and an FNRS Research Director at UCLouvain. Over the past 24 years, he has dedicated his research to advancing ground-penetrating radar (GPR) full-wave modeling and inversion for digital soil mapping and nondestructive testing. His main fundamental contributions in this field include the development of full-wave far-field and near-field radar equations, which have significantly advanced GPR research. He has authored or co-authored over 108 journal articles on these topics and has made numerous other contributions to these fields. His research interests also include remote sensing, hydrogeophysics, road inspection, and gesture recognition.

Dr. Lambot was awarded a European Marie-Curie Post-Doctoral Fellowship and conducted research at Delft University of Technology, The Netherlands, from 2004 to 2005. His expertise in GPR has led to his participation in the organization of several international conferences and workshops, including serving as the General Chair of the Third International Workshop on Advanced Ground Penetrating Radar in 2005 and the 15th International Conference on Ground Penetrating Radar in 2014. More recently, he co-chaired IGARSS 2021. He has also edited several special issues in *Near Surface Geophysics*, *Vadose Zone Journal*, and IEEE JOURNAL OF SELECTED TOPICS IN APPLIED EARTH OBSERVATIONS AND REMOTE SENSING (JSTARS).